

# Master equation-based model for infrared-based magnetometry with nitrogen-vacancy centers in diamond cavities: a path to sub-picotesla sensitivity at sub-millimeter scales

Hadi Zadeh-Haghghi,<sup>1, 2,\*</sup> Omid Golami,<sup>1, 2</sup> Vinaya Kumar Kavatamane,<sup>1, 2</sup> Paul E. Barclay,<sup>1, 2, 3</sup> and Christoph Simon<sup>1, 2, †</sup>

<sup>1</sup>*Department of Physics and Astronomy, University of Calgary, Calgary, AB T2N 1N4, Canada*

<sup>2</sup>*Institute for Quantum Science and Technology, University of Calgary, Calgary, AB T2N 1N4, Canada*

<sup>3</sup>*Nanotechnology Research Centre, National Research Council of Canada, Edmonton, AB T6G 2M9, Canada*

(Dated: July 9, 2024)

Our study aims to increase the spatial resolution of high-sensitivity magnetometry based on singlet-transition infrared (IR) absorption using nitrogen-vacancy (NV) centers in diamonds in monolithic cavities, with potential applications in bio-magnetic field detection. We develop a master-equation treatment of optically detected magnetic resonance, incorporating IR light saturation effects. This master equation provides the singlet population, which is then utilized to calculate the reflectivity and ultimately derive the magnetic field sensitivity taking into account photon and spin shot noise. We further show that our model is compatible with experiments of IR-based NV center magnetometry. Through optimization in a high-parameter space, we uncover the potential to achieve sensitivities in the order of sub-pico tesla, even for sub-millimeter scales.

## I. INTRODUCTION

Detecting minuscule magnetic fields plays a pivotal role in various scientific and technological domains, including geoscience, atmospheric science, atomic and particle physics, (bio)chemistry, and medicine [1, 2]. Quantum sensors, harnessing inherent quantum properties, offer extraordinary precision, repeatability, and accuracy in measurements [3]. These sensors find applications across diverse technologies [1]. While current sensors are already highly sensitive, ongoing technological advancements aim to meet the growing demands in various domains. For instance, applications like magnetocardiography and magnetoencephalography continue to benefit from improvements in both sensitivity and spatial resolution [4, 5].

Such ranges of magneto-sensing have been achieved based on technologies such as optically pumped magnetometers [6, 7], superconducting quantum interference devices (SQUIDs) [8], and tunnelling magnetoresistance sensors [9]. However, these magnetometers typically offer resolutions that are confined to a few centimetres due to limitations in standoff distance or sensor size. Notably, SQUIDs, with their requirement for cryogenic conditions and extended sensor geometries, operate with standoff distances of around a centimetre or more from the biological sample. It is worth mentioning that magnetic resonance force microscopy (MRFM) is an imaging technique that can achieve angstrom spatial resolution but requires non-ambient conditions such as high vacuum [10]. Thus, the next crucial step in advancing magnetometers is to enhance their spatial resolution to sub-centimetre scales.

Among recent sensors, the use of nitrogen-vacancy

(NV) color centers in diamond for magnetometry has gained considerable attention [11–29], as they function under ambient conditions. In the negatively charged NV center in diamond, the transition between the ground and excited triplet states is optically allowed (see Fig. 1) [30]. At room temperature and above, the electron spin resonance of the NV center can be easily observed due to the millisecond-order spin-lattice relaxation time and the fluorescence contrast between the  $m_s = 0$  and  $m_s = \pm 1$  spin sub-levels. Resonant lasers can pump electrons from the ground state to the excited triplet state while conserving their spin. These excited electrons can decay either by emitting a photon or through intersystem crossing to the  $^1A_1$  singlet state, which is non-radiative and non-spin-conserving. From there, the electron decays to the  $^1E$  metastable state by emitting an IR (1042 nm) photon, and then non-radiatively to the ground triplet state. The decay from the spin  $\pm 1$  sub-levels to the singlet state is more pronounced than from the spin 0 sub-level, resulting in a higher probability of non-radiative decay for electrons in the spin  $\pm 1$  sub-levels. Consequently, a green laser will eventually populate the spin-zero sub-level [31]. When microwave radiation resonates with the ground state spin sub-levels, it induces transitions between these sub-levels, reducing fluorescence intensity and causing a dip in the photo-luminescence spectrum. This Optically Detected Magnetic Resonance (ODMR) signal, sensitive to external magnetic fields and temperature, is crucial for sensing applications [32, 33].

Aiming for better resolution in magnetic field detection, recent investigations into microcavity-enhanced NV center magnetometry have shown promise [34]. This method combines the unique properties of NV centers in diamond with enhanced light-matter interaction within microcavities to achieve highly sensitive magnetic field measurements and potential spatial resolution improvements [35–41].

\* [hadi.zadehhaghghi@ucalgary.ca](mailto:hadi.zadehhaghghi@ucalgary.ca)

† [csimo@ucalgary.ca](mailto:csimo@ucalgary.ca)

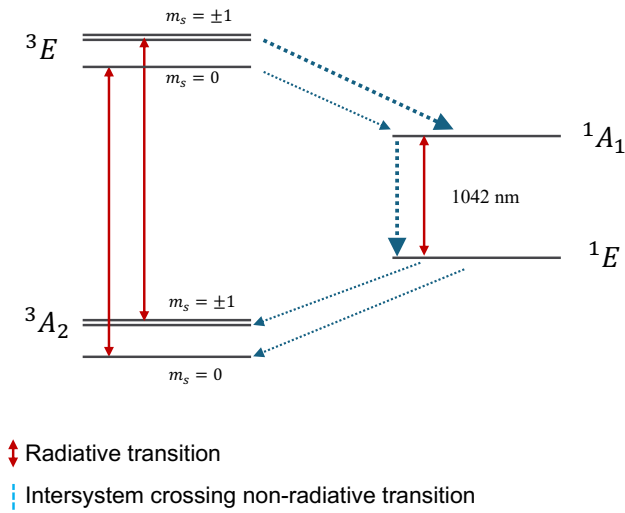


FIG. 1: Electronic structure of the  $\text{NV}^-$  color center in diamond at zero magnetic field. The  ${}^3A_2$  and  ${}^3E$  states are triplet states, while  ${}^1E$  and  ${}^1A_1$  are singlet states. The intersystem crossing from the spin 0 sub-level of the excited triplet state to the singlet state is weaker compared to the intersystem crossing from the spin  $\pm 1$  sub-levels.

Conventional fluorescence-based magnetometer sensitivity is constrained by shot noise due to low fluorescence contrast [24, 42, 43]. One approach to enhance the fidelity of readout in NV-center magnetometry is the readout based on the population in the NV singlet states [44]. At room temperature, the upper singlet state,  $^1A_1$  (See Fig. 1), has a lifetime of  $\lesssim 1$  ns [45, 46] while the lifetime of the lower singlet state,  $^1E_1$ , is  $\sim 140$ -220 ns [45, 47, 48]. The corresponding energy difference between  $^1A_1$  and  $^1E_1$  is 1042 nm. Thus, by applying this wavelength, one can change and monitor the  $^1E_1$  population. In an absorption-based measurement, however, an IR laser is used to probe the changes in the density of the metastable state, which can improve the signal contrast and collection efficiency and thus the sensitivity [44]. Jensen et al. achieved a magnetic field sensitivity of  $70 \text{ pT}/\sqrt{\text{Hz}}$  at room temperature using IR-based cavity-enhanced magnetometry with NV centers in diamond, with the mirror spacing on the order of a few cm [44]. Furthermore, the transition between the singlet states  $^1E$  and  $^1A_1$  demonstrates a saturation intensity ( $I_{\text{sat}}^{1042} \approx 0.5 \text{ W}/\mu\text{m}^2$ ) [29, 49], which did not impose limitation in that work. However, saturation of this transition can result in constraints in particular for smaller cavities. Chatzidrosos et al. [50] achieved a magnetic field sensitivity of  $28 \text{ pT}/\sqrt{\text{Hz}}$  using a sensing volume of  $390 \mu\text{m} \times 4500 \mu\text{m}^2$ .

Previously, for calculating magnetic sensitivity based on IR absorption, the spin density of the levels in NV centers within a cavity was determined using a rate equation, which considered only spin-conserving optical transitions [49]. In this work, we advance the methodology by calculating the spin density of the levels through quantum master equation calculations, providing a more comprehensive description of the system.

hensive and precise understanding of the system’s dynamics. To achieve this, we assume a model integrating diamond within a Fabry–Pérot cavity and explore the effects of cavity properties on sensitivity for a given spatial resolution. Our approach is in a reasonable agreement with the experimental observation for larger cavities by Chatzidrosos et al. [50]. We also use the differential evolution method [51] to find the optimized range of hyperparameters to achieve the best possible sensitivity.

This paper is organized as follows: In section II, we use ODMR studies to calculate IR absorption of NV center in diamond. Next, we calculated the transmitted and reflected light intensities using a Fabry-Pérot cavity model, including IR absorption, and quality factor corresponding to the intrinsic losses. Based on these findings and incorporating saturation limits and input power, we calculate the sensitivity of the NV center in the cavity. Section III discusses further aspects of this research.

## II. RESULTS

### A. The spin dynamics

In NV centers even when there is no external magnetic field present, the  $m_s = 0$  and  $m_s = \pm 1$  states are non-degenerate due to the strong dipolar interaction between electronic spins, known as zero-field interaction or zero-field splitting. The spin Hamiltonian of the system in the eigenframe reads as follows:

$$\hat{H} = \sum_{i=x,y,z} D_i \hat{S}_i^2 = D \left( \hat{S}_z^2 - \frac{1}{3} S(S+1) \right) + E(\hat{S}_x^2 - \hat{S}_y^2) + \mu_B g_e \hat{S}_z B_z, \quad (1)$$

where the axial component of the magnetic dipole-dipole interaction  $D = \frac{3}{2}D_z$  and the transversal component  $E = \frac{D_x - D_y}{2}$ .  $\mu_B$  and  $g_e$  are the Bohr magneton and the electron gyromagnetic ratio, respectively.  $D$  describes the axial component of the magnetic dipole-dipole interaction, and  $E$  the transversal component

We obtain the time evolution of the density matrix by using the Lindblad master equation:

$$\frac{d\hat{\rho}}{dt} = \mathcal{L}\hat{\rho} = -i[H, \hat{\rho}] + \sum_{i=1}^N \gamma_i [L_i \hat{\rho} L_i^\dagger - \frac{1}{2} \{L_i^\dagger L_i, \hat{\rho}\}], \quad (2)$$

where the jump operators  $L_i$  and their corresponding rates  $\gamma_i$ , as defined in Table I.

## B. Absorption-based optically detected magnetic resonance

In this work, we focus on the absorption-based approach, where the ODMR signal is given by the absorption contrast of an IR driving laser. Therefore, using

Operator	Matrix Element	Rate
<b>Optical Transitions</b>		
$L_1$	$ 1\rangle\langle 4 $	$\gamma_1 = k_{41}$
$L_2$	$ 2\rangle\langle 5 $	$\gamma_2 = k_{52}$
$L_3$	$ 3\rangle\langle 6 $	$\gamma_3 = k_{63}$
$L_4$	$ 4\rangle\langle 1 $	$\gamma_4 = k_{41} + W_p$
$L_5$	$ 5\rangle\langle 2 $	$\gamma_5 = k_{52} + W_p$
$L_6$	$ 6\rangle\langle 3 $	$\gamma_6 = k_{63} + W_p$
$L_7$	$ 7\rangle\langle 8 $	$\gamma_7 = k_{87}$
$L_8$	$ 8\rangle\langle 7 $	$\gamma_8 = k_{87}$
<b>Spin Transitions</b>		
$L_9$	$ 1\rangle\langle 2 $	$\gamma_9 = \gamma_{gMW}$
$L_{10}$	$ 2\rangle\langle 1 $	$\gamma_{10} = \gamma_{gMW}$
$L_{11}$	$ 1\rangle\langle 3 $	$\gamma_{11} = \gamma_{gMW}$
$L_{12}$	$ 3\rangle\langle 1 $	$\gamma_{12} = \gamma_{gMW}$
$L_{13}$	$ 4\rangle\langle 5 $	$\gamma_{13} = \gamma_{eMW}$
$L_{14}$	$ 5\rangle\langle 4 $	$\gamma_{14} = \gamma_{eMW}$
$L_{15}$	$ 4\rangle\langle 6 $	$\gamma_{15} = \gamma_{eMW}$
$L_{16}$	$ 6\rangle\langle 4 $	$\gamma_{16} = \gamma_{eMW}$
<b>Dephasing</b>		
$L_{17}$	$ 2\rangle\langle 2 $	$\gamma_{17} = 2\gamma_\Phi$
$L_{18}$	$ 3\rangle\langle 3 $	$\gamma_{18} = 2\gamma_\Phi$
$L_{19}$	$ 5\rangle\langle 5 $	$\gamma_{19} = 2\gamma_\Phi$
$L_{20}$	$ 6\rangle\langle 6 $	$\gamma_{20} = 2\gamma_\Phi$
<b>Metastable States</b>		
$L_{21}$	$ 8\rangle\langle 4 $	$\gamma_{21} = k_{48}$
$L_{22}$	$ 8\rangle\langle 5 $	$\gamma_{22} = k_{58}$
$L_{23}$	$ 8\rangle\langle 6 $	$\gamma_{23} = k_{68}$
$L_{24}$	$ 7\rangle\langle 1 $	$\gamma_{24} = k_{71}$
$L_{25}$	$ 7\rangle\langle 2 $	$\gamma_{25} = k_{72}$
$L_{26}$	$ 7\rangle\langle 3 $	$\gamma_{26} = k_{73}$

TABLE I: Summary of jump operators.  $k_{41} = k_{52} = k_{63} = 66$  MHz,  $k_{87} = 1$  GHz,  $k_{48} = 7.9$  MHz,  $k_{58} = k_{68} = 53$  MHz,  $k_{72} = k_{73} = 0.7$  MHz,  $k_{71} = 1$  MHz,  $W_p = 1$  MHz,  $\gamma_{gMW} = 1$  kHz, and  $\gamma_\Phi = 1$  MHz [49].

Eq. 2, we simulate the absorption-based ODMR signal by introducing an IR pump. For this, we use a jump operator corresponding to optical absorption,  $L_{7/8}$ . Our simulation of the absorption-based ODMR signal for our setup (Rabi frequency  $\Omega_R = 5$  MHz,  $T_2^* = 500$  ns) is presented in Fig. 2(a). The ODMR contrast for this setup is approximately 58.36%, representing the increase in absorbed IR photons compared to when the MW drive is far detuned.

Moreover, this approach enables us to calculate a more realistic steady-state density of states for the electronic structure of the NV<sup>-</sup> center, taking into account the decoherence mechanisms that influence it. This density of states is subsequently used in the calculations of magnetic field sensitivity, which are discussed in the following section.

To simulate the ODMR signal, we initially compared a fluorescence-based signal from a single NV center with experimental data to assess the accuracy of our theoretical model in reproducing the results. Fig. 2(b) presents the ODMR contrast as a function of  $s$  the saturation parameter  $s = P_{in}/P_{sat}$ , where  $P_{in}$  and  $P_{sat}$  are the optical pumping power and the saturation power of the transition, respectively and  $P_{sat}=25$  MHz, based on the setup

in Dréau et al. [52].

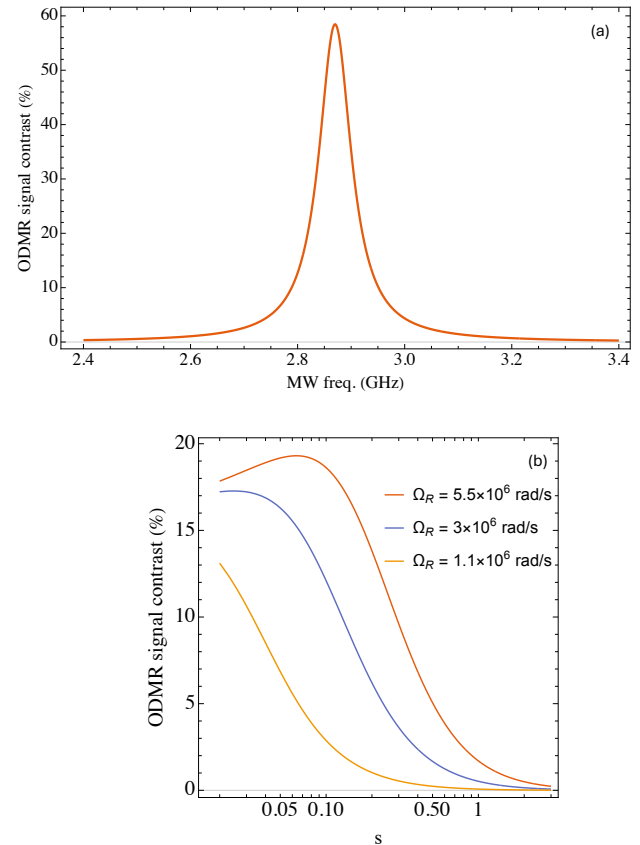


FIG. 2: (a) The IR absorption ODMR signal for a single NV at zero static (bias) magnetic field. (b) ODMR contrast as a function of  $s = P_{in}/P_{sat}$ , where  $P_{in}$  and  $P_{sat}$  are the optical pumping power and the saturation power of the transition, respectively and  $P_{sat}=25$  MHz

, based on the setup in Dréau et al. [52].

### C. Magnetic field and NV orientations

In the presence of an external magnetic field, due to Zeeman interaction the spin  $\pm 1$  sub-levels will split, and there will be two resonance peaks in the ODMR signal. Additionally, if we consider four different orientations of NV centers in the diamond crystal, these peaks will be split into more peaks. In the case of aligning the external magnetic field with one of these directions, there will be four peaks; two caused by contributions from the aligned NVs, and two from three other orientations. If we assume that NV centers are distributed uniformly between these four orientations, two peaks corresponding to the aligned NVs (first and last peaks in Fig. 3 (a)) will have a third of the contrast from the other three orientations.

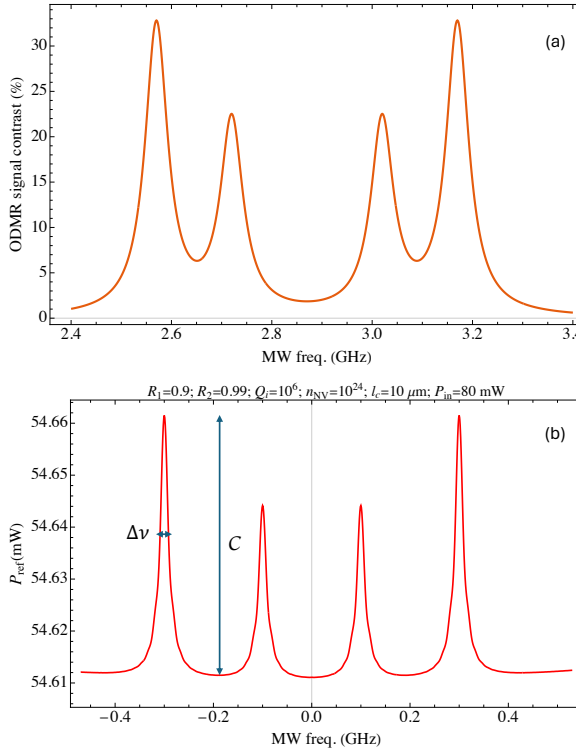


FIG. 3: (a) The ODMR signal where an external magnetic field is aligned with the direction of one of the four possible NV orientations in the diamond crystal. (b) The reflected light power,  $P_{ref}$ , in the presence of NV centers with the incoming light power of  $P_{in} = 80\ \text{mW}$ . The contrast  $C$  is the contrast and  $\Delta\nu$  is the full width at half maximum of the magnetic resonances.

#### D. Magnetometry

For the cavity, we consider the Fabry-Pérot cavity model with two distinct mirrors, with reflectivities of  $R_1$  and  $R_2$ , cavity lengths of  $\ell_c$ , and light with wavelength of  $\lambda$ . In this model, we also consider background loss,  $a \equiv a(\ell_c, Q_i) = \frac{\ell_c}{\lambda Q_i}$ , where  $Q_i$  is the quality factor corresponding to the background loss.

For sensitivity calculation, our readout is the population difference between the singlet ground ( ${}^1E_1$ ) and excited ( ${}^1A_1$ ) states,  $\Delta\rho$ . We incorporated them into the reflected light intensity. Through this, we also included the saturation limit in terms of IR Rabi frequency, where the excited state population becomes comparable to the ground state population. This IR absorption depends on multiple factors such as NV center density ( $n_{NV}$ ), and absorption cross-section ( $\sigma_{NV}$ ). This can be denoted as optical depth  $d = n_{NV}\ell_c\sigma_{NV}\Delta\rho$ . The reflected light power intensity reads as follows:

$$P_{ref} = \frac{P_{in}(\sqrt{R_1} - \sqrt{R_2}e^{-(a+d)})^2 + 4\sqrt{R_1R_2}e^{-(a+d)}\sin^2\phi}{(1 - \sqrt{R_1R_2}e^{(a+d)})^2 + 4\sqrt{R_1R_2}e^{-(a+d)}\sin^2\phi}, \quad (3)$$

where  $P_{in}$  and  $\nu$  are the incoming light power intensity and the light frequency, respectively, and  $\phi = 2\pi\nu$ .

The normalized reflected light,  $P_{ref}$  in the presence of NV centers and IR absorption (for  $R_1 = 0.9$ ,  $R_2 = 0.99$ ,  $Q_i = 10^6$ ,  $n_{NV} = 10^{24}\ \text{m}^{-3}$ , the incoming light power  $P_{in} = 80\ \text{mW}$ , and  $\ell_c = 10^{-5}\ \text{m}$ ) is shown in Fig. 3 (b).

The circulating light intensity in the cavity can be written as

$$I_{cir} = \frac{I_{inc}(1 - R_1)e^{-(a+d)}}{(1 - \sqrt{R_1R_2}e^{-(a+d)})^2 + 4\sqrt{R_1R_2}e^{-(a+d)}\sin^2\phi}. \quad (4)$$

The magnetic field sensitivity of the cavity with NV centers,  $\delta B$ , can be estimated based on the minimum detectable magnetic field during an acquisition time taking into account photon shot noise, which depends on the contrast,  $C$ , and the full width at half maximum,  $\Delta\nu$ , of the magnetic resonances [44, 53], as shown in Fig. 3 (b):

$$\delta B = \frac{2\pi\Delta\nu}{\gamma C}\sqrt{\frac{h\nu}{P}}, \quad (5)$$

where  $h$ , and  $\nu$ ,  $\gamma = 1.761 \times 10^{11}\ \text{rad s}^{-1}\ \text{T}^{-1}$  are, respectively, the Planck constant, photon frequency (IR light 1042 nm), and the gyromagnetic ratio.

We also considered the spin shot noise limit [49],

$$\delta B_s = \frac{2}{\gamma\sqrt{n_{NV}\ell_c\sigma_m T_2^* t_m}}, \quad (6)$$

where  $\sigma_m$  and  $t_m$  are, respectively, the mode size and measurement time, and we ensured that it was at most 20% of  $\delta B$ , where  $T_2^* = 2/\Delta\nu$ .

In their research on IR-based magnetometry, Chatzidrosos et al. utilized a cavity composed of two mirrors with reflectivities of  $R_1 = 98.5\%$  and  $R_2 = 99.2\%$  at 5 mm from each other, a 0.39 mm diamond length featuring a high NV center density of  $28 \times 10^{23}\ \text{m}^{-3}$ , and an input power of  $P_{in} = 80\ \text{mW}$  [50]. This setup enabled them to achieve a magnetic field sensitivity of  $28\ \text{pT}/\sqrt{\text{Hz}}$  with a spin noise of  $\sim 0.46\ \text{pT}/\sqrt{\text{Hz}}$ . To validate our model, we aim to reproduce their achieved magnetic field sensitivity based on the used setup. As our model treats the cavity length as the diamond length, we explored two cases. In the first case, we considered that the cavity's length is the same as their diamond, where we used  $28 \times 10^{23}\ \text{m}^{-3}$  as the NV center density. For this case, our model resulted in  $5\ \text{pT}/\sqrt{\text{Hz}}$ . For the second case, we used a cavity length similar to theirs but set the NV center density to an effective value of  $2.18 \times 10^{23}\ \text{m}^{-3}$  in order to match the optical depth per pass in their experiment. Our model, for this set, gave a sensitivity of  $2.5\ \text{pT}/\sqrt{\text{Hz}}$ . Based on this theoretical model, the spin noise was  $\sim 0.25\ \text{pT}/\sqrt{\text{Hz}}$ . Our model predicts somewhat better sensitivity than is observed experimentally, which is likely due to a combination of the monolithic character of the cavity in our model, as well as additional technical noise

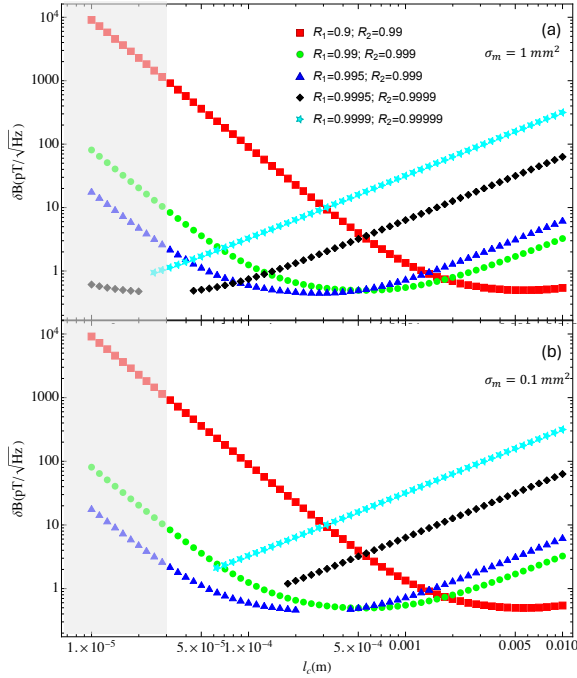


FIG. 4: Magnetic Field Sensitivity vs Cavity Length. The sensitivity vs the cavity length is calculated for different mirror reflectivities (see legend) for input power of 1 W, quality factor of  $10^6$ , NV density of  $10^{24} \text{ m}^{-3}$ , and mode cross-section of  $1 \text{ mm}^2$  (a) and  $0.1 \text{ mm}^2$  (b). Here, the intra-cavity intensity is below the saturation limit of  $0.5 \text{ W}/\mu\text{m}^2$ . The spin shot noise limit is below 20% of the photon shot noise. The gray area indicated lengths smaller than  $\sim 30 \mu\text{m}$  ( $10 \mu\text{m}$  diameter for micro-cavity).

sources in the experiment in addition to photon shot noise and spin shot noise.

Using Eq. 5, to achieve the optimal values, we have explored different values for the mirrors reflectivities, intrinsic loss, NV center density, and cavity length and cross-section. Optimizing hyperparameters for a cavity-based sensing system presents a complex challenge due to the inherently non-linear nature of the parameters in this problem. To address this complexity, we employed the Differential Evolution algorithm [51]. Additionally, we accounted for constraints imposed by spin noise and the saturation limits of the system, ensuring that the optimization process remained grounded in the physical realities of the sensing mechanism. Here, the intra-cavity intensity is constrained by the saturation intensity  $0.5 \text{ W}/\mu\text{m}^2$  [44]. In this work, we set the spin shot noise limit to be below 20% of the photon shot noise unless stated otherwise.

Fig. 4 shows the sensitivity as a function of the cavity length for different mirror reflectivities and different cavity dimensions, where the spin noise and intra-cavity saturations limits were imposed. Notably, Fig. 4 demonstrates that the sub-pT sensitivity is achievable over a wide range of cavity lengths.

For experimental implementation purposes, by fixing the quality factor, input power, cavity length, and NV center density, we explored the impact of mirrors' reflectivities, as shown in Fig. 5. For a length of 1 cm and 50

$\mu\text{T}$ , the sensitivity can reach sub-pico tesla. For a smaller cavity, even higher reflectivities are required for achieving the same order of sensitivity (Fig. 5b). Further hyperparameter exploration can be found in the Appendix.

We also explored scenarios where the NV center density in diamond were  $10^{21} \text{ m}^{-3}$  and  $10^{18} \text{ m}^{-3}$ , as shown in Figs. 6(a-c) and 6(d), respectively. Having lower NV center densities results in higher spin noise. For  $10^{21} \text{ m}^{-3}$ , to achieve sub-pico tesla one needs larger cavity lengths. To get the same order of sensitivity, using  $10^{18} \text{ m}^{-3}$  requires not only larger cavity lengths, but also we had to allow the spin noise to become equal to the photon shot noise.

### III. DISCUSSION

In this study, we explored the potential of using diamond-based Fabry-Pérot cavities for enhancing the performance of magnetometry using NV centers based on IR absorption of the singlet states. Using the Lindblad master equation, we calculated the population of singlet states, including the saturation limits. The master equation gives us the singlet population, which we then feed into the calculation of the reflectivity, from which we derive the magnetic field sensitivity. Using the differential evolution algorithm, we were able to explore the hyperparameter space, including mirror reflectivities, cavity length, cross-section mode size, quality factor, input power, and NV center density. For this optimization search, we also imposed the constraints due to the saturation and spin noise limitations. This analysis shows that even for smaller cavities, one can achieve high sensitivities of sub-pico tesla.

Of note, in our calculations, we specifically considered the length of the Fabry-Perot cavity to be equivalent to the length of the diamond, a scenario typical for NV centers in diamond within microcavities. This is a valid assumption for monolithic cavities. However, for free-space Fabry-Perot cavities, where the cavity length may not necessarily match the medium length there can be additional reflections at the interfaces (e.g., diamond), further care must be exercised.

Our model allows for several exciting extensions and opportunities for further research. One promising direction is the experimental exploration of microcavities, which could enhance the performance of NV center-based magnetometry by achieving higher sensitivities and spatial resolutions. Potential applications of these advanced sensors are vast and varied. In medical diagnostics, highly sensitive NV center-based magnetometers could enhance techniques such as magnetocardiography and magnetoencephalography, enabling non-invasive, high-resolution imaging of cardiac and neural activity. The ongoing optimization and experimental validation of our model will be key to realizing these applications.

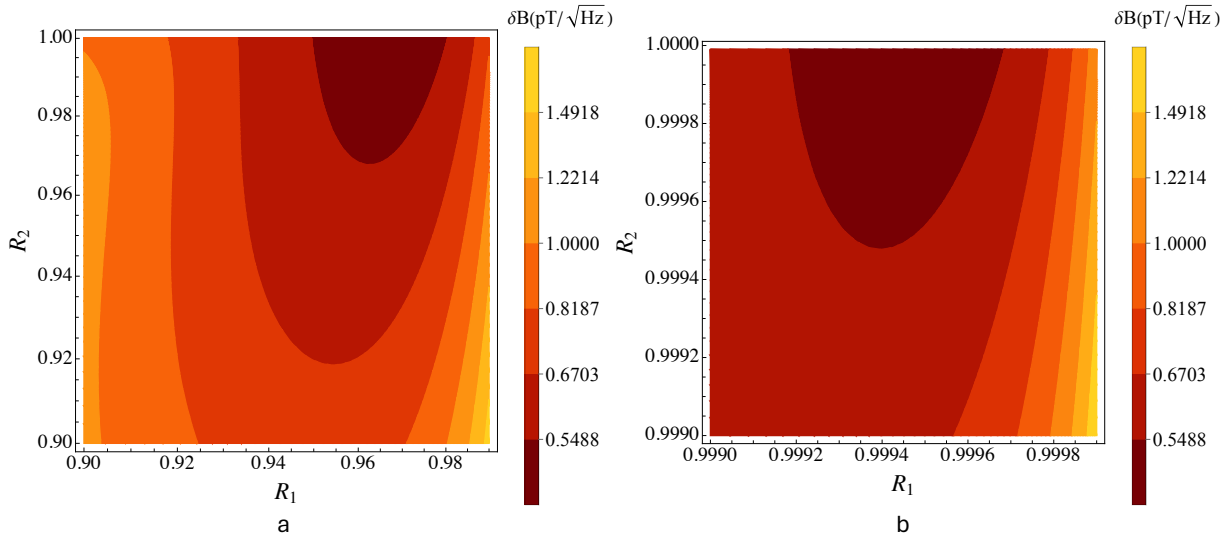


FIG. 5: Magnetic-field sensitivity as a function of the two mirror reflectivities for different dimensions, (a) with the cavity length of 3 mm and mode cross-section of  $1 \text{ cm}^2$  and (b) with the cavity length of  $50 \mu\text{m}$  and mode cross-section of  $1 \text{ mm}^2$ . Both cases can achieve sub-pico tesla sensitivity. For such sensitivity having smaller dimensions requires higher mirror reflectivities. In both cases, the intra-cavity intensity is below the saturation limit of  $0.5 \text{ W}/\mu\text{m}^2$  and the spin shot noise limit is below 20% of the photon shot noise. The cavity quality factor, NV density in diamond, and input power are  $10^6$ ,  $10^{24} \text{ m}^{-3}$ , and 1 W, respectively.

## ACKNOWLEDGMENT

The authors thank Erika Janitz and Faezeh Kimiaeef Asadi for helpful discussions. This work was supported by an NSERC/Alberta Innovates Advance Grant.

## IV. APPENDIX

Fixing mirrors' reflectivities, input power, quality factor, and mode cross-section size, we searched the cavity length and NV center density in diamond, considering the limitations due to the noise and intensity saturation in the cavity, the sensitivity can reach to a sub  $\text{pT}/\sqrt{\text{Hz}}$ , as shown in Fig. 7. We also looked at other cases where for having higher sensitivity and smaller cavities higher mirror reflectivities are required. Further, we investigated extreme cases where the input power was considered as a variable and cavity size of  $10 \mu\text{m}$  and mode cross-section of  $100 \mu\text{m}^2$ . Due to the saturation and noise limits resulted in sensitivities order of a sub  $\text{pT}/\sqrt{\text{Hz}}$ , as shown in Fig. 7c.

---

[1] C. Degen, F. Reinhard, and P. Cappellaro, *Reviews of Modern Physics* **89** (2017), 10.1103/revmodphys.89.035002.

[2] P. Ripka and M. Janosek, *IEEE Sensors Journal* **10**, 1108–1116 (2010).

[3] D. Budker and M. Romalis, *Nature Physics* **3**, 227 (2007).

[4] K. Arai, A. Kuwahata, D. Nishitani, I. Fujisaki, R. Matsuki, Y. Nishio, Z. Xin, X. Cao, Y. Hatano, S. Onoda, C. Shinei, M. Miyakawa, T. Taniguchi, M. Yamazaki, T. Teraji, T. Ohshima, M. Hatano, M. Sekino, and T. Iwasaki, *Communications Physics* **5** (2022), 10.1038/s42005-022-00978-0.

[5] S. Baillet, *Nature Neuroscience* **20**, 327 (2017).

[6] Y. J. Kim and I. Savukov, *Scientific Reports* **6** (2016), 10.1038/srep24773.

[7] S. Zhang, J. Lu, M. Ye, Y. Zhou, K. Yin, F. Lu, Y. Yan, and Y. Zhai, *IEEE Transactions on Instrumentation and Measurement* **71**, 1 (2022).

[8] J.-H. Storm, P. Hömmen, D. Drung, and R. Körber, *Applied Physics Letters* **110** (2017), 10.1063/1.4976823.

[9] J. Gao, J. Wang, Y. Shen, Z. Jiang, Y. Huang, and Q. Yu, *IEEE Electron Device Letters* **41**, 1400 (2020).

[10] D. Rugar, R. Budakian, H. J. Mamin, and B. W. Chui, *Nature* **430**, 329–332 (2004).

[11] R. Schirhagl, K. Chang, M. Loretz, and C. L. Degen, *Annual Review of Physical Chemistry* **65**, 83 (2014).

[12] G. Kucska, P. C. Maurer, N. Y. Yao, M. Kubo, H. J. Noh, P. K. Lo, H. Park, and M. D. Lukin, *Nature* **500**, 54–58 (2013).

[13] I. Lovchinsky, A. O. Sushkov, E. Urbach, N. P. de Leon, S. Choi, K. D. Greve, R. Evans, R. Gertner, E. Bersin,

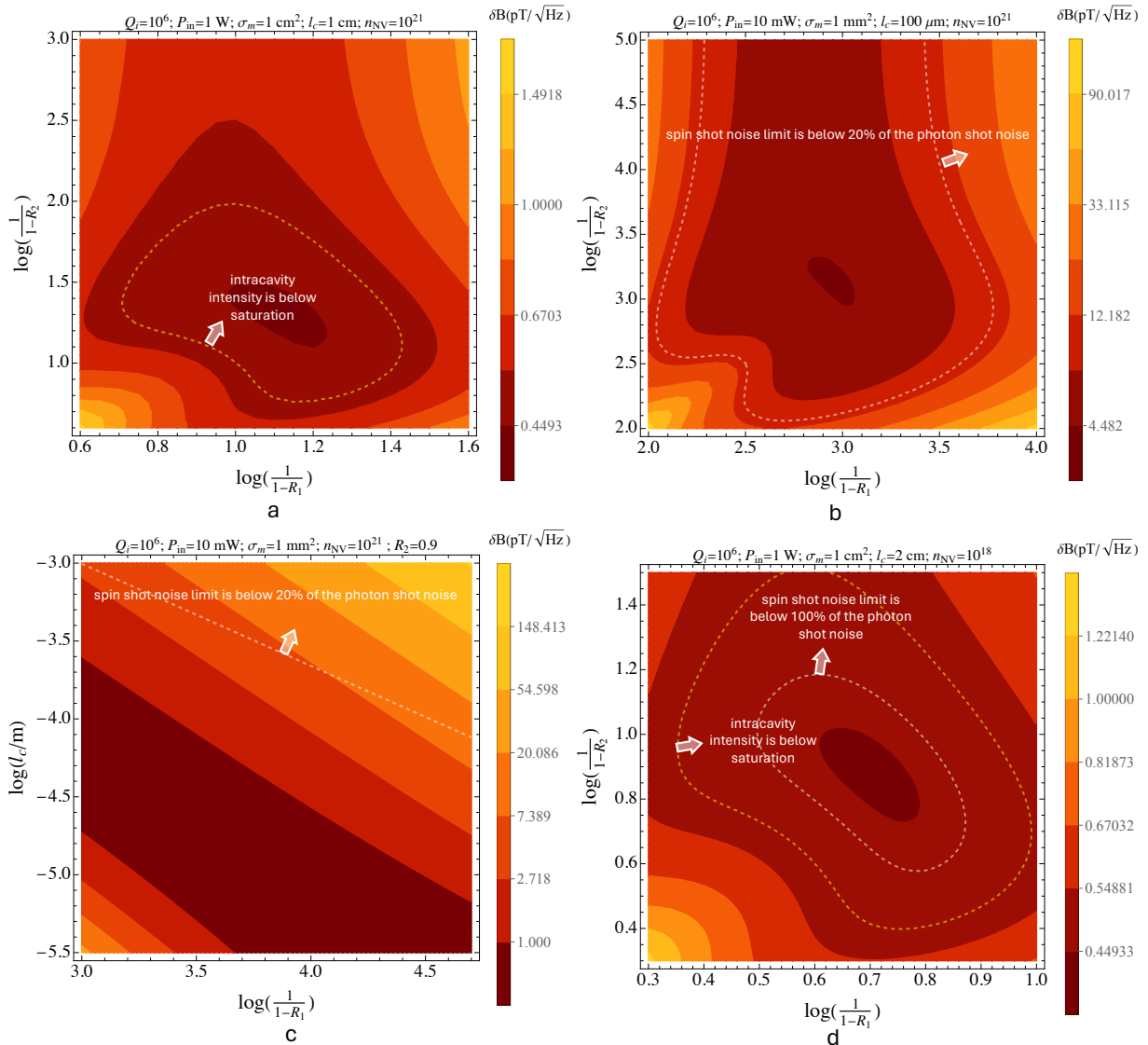


FIG. 6: Sensitivity for lower NV densities. Magnetic-field sensitivity on the mirrors' reflectivities (a) and (b) and on mirror-1 reflectivity and cavity length (c) for NV density of  $10^{21}$  m $^{-3}$ . The dashed lines indicate the parameter region where the spin shot noise limit is below 20% of the photon shot noise. (d) Magnetic-field sensitivity on the mirrors' reflectivities for the cavity length for NV density in diamond of  $10^{18}$  m $^{-3}$ . The inner dashed line indicated the region where the spin noise shot is below 100% of the photon shot noise. The Larger dashed line indicated the region where the intra-cavity light intensity is below the saturation limit of  $0.5$  W/ $\mu$ m $^2$ . In all cases, the absence of the dashed lines for both constrains implies that the condition are satisfied.

C. Müller, L. McGuinness, F. Jelezko, R. L. Walsworth, H. Park, and M. D. Lukin, *Science* **351**, 836 (2016).

[14] J. F. Barry, M. J. Turner, J. M. Schloss, D. R. Glenn, Y. Song, M. D. Lukin, H. Park, and R. L. Walsworth, *Proceedings of the National Academy of Sciences* **113**, 14133–14138 (2016).

[15] Y. Wu, F. Jelezko, M. B. Plenio, and T. Weil, *Angewandte Chemie International Edition* **55**, 6586 (2016).

[16] D. R. Glenn, R. R. Fu, P. Kehayias, D. L. Sage, E. A. Lima, B. P. Weiss, and R. L. Walsworth, *Geochemistry, Geophysics, Geosystems* **18**, 3254 (2017).

[17] F. Casola, T. van der Sar, and A. Yacoby, *Nature Reviews Materials* **3** (2018), 10.1038/natrevmats.2017.88.

[18] F. Shi, F. Kong, P. Zhao, X. Zhang, M. Chen, S. Chen, Q. Zhang, M. Wang, X. Ye, Z. Wang, Z. Qin, X. Rong, J. Su, P. Wang, P. Z. Qin, and J. Du, *Nature Methods* **15**, 697–699 (2018).

[19] G.-Q. Liu, X. Feng, N. Wang, Q. Li, and R.-B. Liu, *Nature Communications* **10** (2019), 10.1038/s41467-019-09327-2.

[20] C.-F. Liu, W.-H. Leong, K. Xia, X. Feng, A. Finkler, A. Denisenko, J. Wrachtrup, Q. Li, and R.-B. Liu, *National Science Review* **8** (2020), 10.1093/nsr/nwaa194.

[21] C. Li, R. Soleyman, M. Kohandel, and P. Cappellaro, *Nano Letters* **22**, 43–49 (2021).

[22] G. Wolfowicz, F. J. Heremans, C. P. Anderson, S. Kanai, H. Seo, A. Gali, G. Galli, and D. D. Awschalom, *Nature Reviews Materials* **6**, 906–925 (2021).

[23] V. V. Soshenko, S. V. Bolshedvorskii, O. Rubinas, V. N. Sorokin, A. N. Smolyaninov, V. V. Vorobiov, and

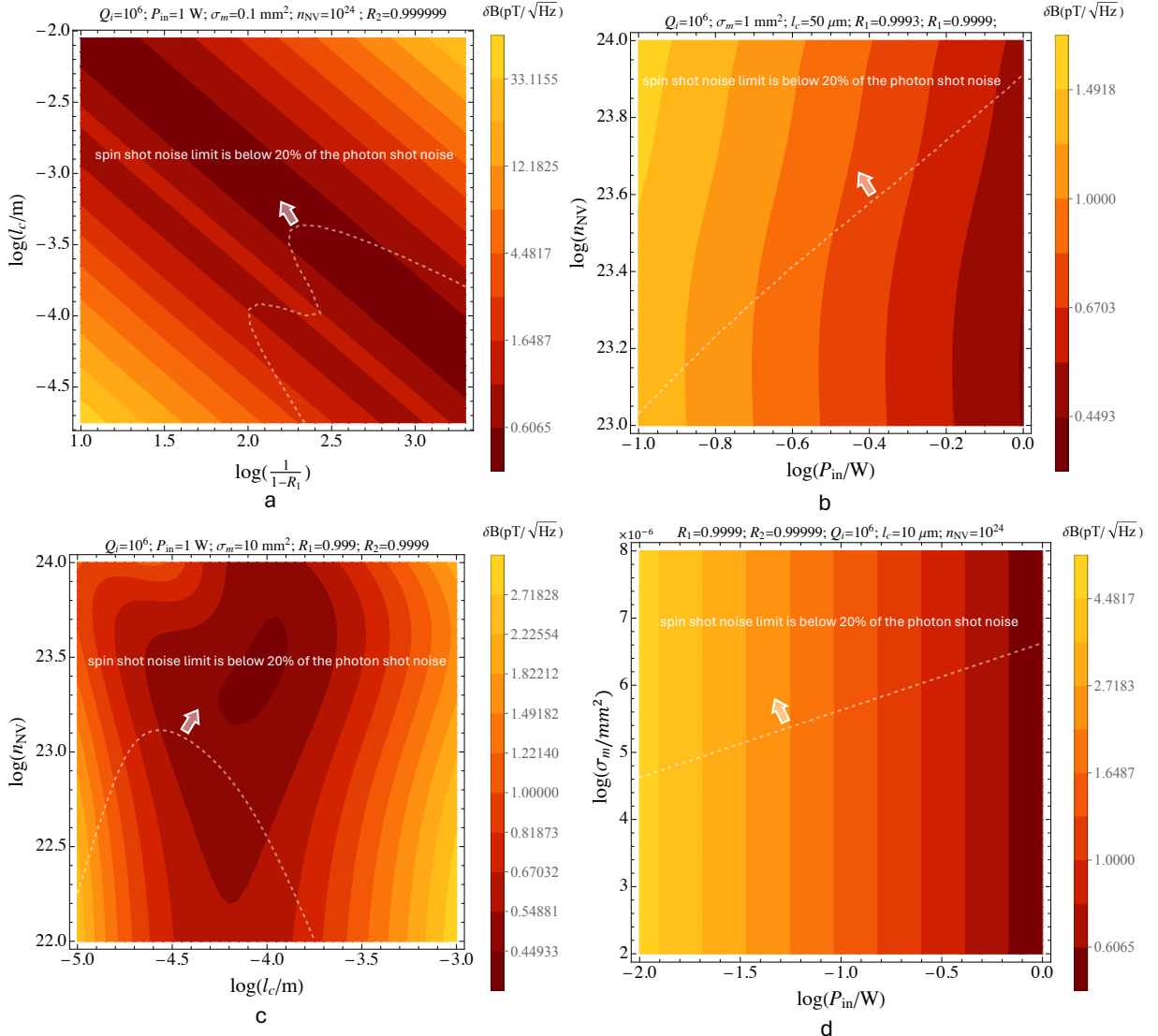


FIG. 7: Sensitivity dependence on various combinations of parameters. The sensitivity (a) on mirror-1 reflectivity and cavity length, (b) on the NV density in diamond and input power, (c) on NV center density in diamond and cavity length, and (d) on mode cross-section and input power. In all case the sensitivity can reach to sub-pico tesla. The dashed lines indicate the parameter region where the spin shot noise limit is below 20% of the photon shot noise. In all cases, the absence of the dashed lines for both constrains implies that the condition are satisfied.

- A. V. Akimov, *Physical Review Letters* **126** (2021), [10.1103/physrevlett.126.197702](https://doi.org/10.1103/physrevlett.126.197702).
- [24] T. Zhang, G. Pramanik, K. Zhang, M. Gulka, L. Wang, J. Jing, F. Xu, Z. Li, Q. Wei, P. Cigler, and Z. Chu, *ACS Sensors* **6**, 2077–2107 (2021).
- [25] F. A. Hahl, L. Lindner, X. Vidal, T. Luo, T. Ohshima, S. Onoda, S. Ishii, A. M. Zaitsev, M. Capelli, B. C. Gibson, A. D. Greentree, and J. Jeske, *Science Advances* **8** (2022), [10.1126/sciadv.abn7192](https://doi.org/10.1126/sciadv.abn7192).
- [26] J. H. Shim, S.-J. Lee, S. Ghimire, J. I. Hwang, K.-G. Lee, K. Kim, M. J. Turner, C. A. Hart, R. L. Walsworth, and S. Oh, *Physical Review Applied* **17** (2022), [10.1103/physrevapplied.17.014009](https://doi.org/10.1103/physrevapplied.17.014009).
- [27] B. L. Dwyer, L. V. Rodgers, E. K. Urbach, D. Bluvstein, S. Sangawesin, H. Zhou, Y. Nassab, M. Fitzpatrick, Z. Yuan, K. De Greve, E. L. Peterson, H. Knowles, T. Sumarac, J.-P. Chou, A. Gali, V. Dobrovitski, M. D. Lukin, and N. P. de Leon, *PRX Quantum* **3** (2022), [10.1103/prxquantum.3.040328](https://doi.org/10.1103/prxquantum.3.040328).
- [28] Z. Wang, F. Kong, P. Zhao, Z. Huang, P. Yu, Y. Wang, F. Shi, and J. Du, *Science Advances* **8** (2022), [10.1126/sciadv.abq8158](https://doi.org/10.1126/sciadv.abq8158).
- [29] J. F. Barry, J. M. Schloss, E. Bauch, M. J. Turner, C. A. Hart, L. M. Pham, and R. L. Walsworth, *Reviews of Modern Physics* **92** (2020), [10.1103/revmodphys.92.015004](https://doi.org/10.1103/revmodphys.92.015004).
- [30] M. W. Doherty, N. B. Manson, P. Delaney, and L. C. L. Hollenberg, *New Journal of Physics* **13**, 025019 (2011).
- [31] P. Kehayias, “Exploring basic properties and applications of nitrogen-vacancy color centers in diamond,”

(2018).

[32] P. Siyushev, H. Pinto, M. Vörös, A. Gali, F. Jelezko, and J. Wrachtrup, *Physical Review Letters* **110** (2013), 10.1103/physrevlett.110.167402.

[33] M. W. Doherty, N. B. Manson, P. Delaney, F. Jelezko, J. Wrachtrup, and L. C. Hollenberg, *Physics Reports* **528**, 1 (2013).

[34] L. Kim, H. Choi, M. E. Trusheim, H. Wang, and D. R. Englund, *Nanophotonics* **12**, 441–449 (2023).

[35] K. J. Vahala, *Nature* **424**, 839 (2003).

[36] J. R. Maze, P. L. Stanwix, J. S. Hodges, S. Hong, J. M. Taylor, P. Cappellaro, L. Jiang, M. V. G. Dutt, E. Togan, A. S. Zibrov, A. Yacoby, R. L. Walsworth, and M. D. Lukin, *Nature* **455**, 644 (2008).

[37] M. Aspelmeyer, T. J. Kippenberg, and F. Marquardt, *Reviews of Modern Physics* **86**, 1391 (2014).

[38] A. Faraon, P. E. Barclay, C. Santori, K.-M. C. Fu, and R. G. Beausoleil, *Nature Photonics* **5**, 301 (2011).

[39] J. Tisler, G. Balasubramanian, B. Naydenov, R. Kolesov, B. Grotz, R. Reuter, J.-P. Boudou, P. A. Curmi, M. Sennour, A. Thorel, M. Börsch, K. Aulenbacher, R. Erdmann, P. R. Hemmer, F. Jelezko, and J. Wrachtrup, *ACS Nano* **3**, 1959 (2009).

[40] P. E. Barclay, K.-M. C. Fu, C. Santori, and R. G. Beausoleil, *Applied Physics Letters* **95**, 191115 (2009).

[41] C. Santori, P. E. Barclay, K.-M. C. Fu, R. G. Beausoleil, S. Spillane, and M. Fisch, *Nanotechnology* **21**, 274008 (2010).

[42] J. Wang, F. Feng, J. Zhang, J. Chen, Z. Zheng, L. Guo, W. Zhang, X. Song, G. Guo, L. Fan, C. Zou, L. Lou, W. Zhu, and G. Wang, *Physical Review B* **91** (2015), 10.1103/physrevb.91.155404.

[43] L. Xu, H. Yuan, N. Zhang, J. Zhang, G. Bian, P. Fan, M. Li, C. Zhang, Y. Zhai, and J. Fang, *Optics Express* **27**, 10787 (2019).

[44] K. Jensen, N. Leefer, A. Jarmola, Y. Dumeige, V. Acosta, P. Kehayias, B. Patton, and D. Budker, *Physical Review Letters* **112** (2014), 10.1103/physrevlett.112.160802.

[45] V. M. Acosta, E. Bauch, A. Jarmola, L. J. Zipp, M. P. Ledbetter, and D. Budker, *Applied Physics Letters* **97**, 174104 (2010).

[46] R. Ulbricht and Z.-H. Loh, *Physical Review B* **98** (2018), 10.1103/physrevb.98.094309.

[47] L. Robledo, H. Bernien, T. v. d. Sar, and R. Hanson, *New Journal of Physics* **13**, 025013 (2011).

[48] A. Gupta, L. Hacquebard, and L. Childress, *Journal of the Optical Society of America B* **33**, B28 (2016).

[49] Y. Dumeige, M. Chipaux, V. Jacques, F. Treussart, J.-F. Roch, T. Debuisschert, V. M. Acosta, A. Jarmola, K. Jensen, P. Kehayias, and D. Budker, *Physical Review B* **87** (2013), 10.1103/physrevb.87.155202.

[50] G. Chatzidrosos, A. Wickenbrock, L. Bougas, N. Leefer, T. Wu, K. Jensen, Y. Dumeige, and D. Budker, *Physical Review Applied* **8** (2017), 10.1103/physrevapplied.8.044019.

[51] P. Rocca, G. Oliveri, and A. Massa, *IEEE Antennas and Propagation Magazine* **53**, 38–49 (2011).

[52] A. Dréau, M. Lesik, L. Rondin, P. Spinicelli, O. Arcizet, J.-F. Roch, and V. Jacques, *Physical Review B* **84** (2011), 10.1103/physrevb.84.195204.

[53] J. M. Taylor, P. Cappellaro, L. Childress, L. Jiang, D. Budker, P. R. Hemmer, A. Yacoby, R. Walsworth, and M. D. Lukin, *Nature Physics* **4**, 810 (2008)